Journal of Alloys and Compounds 820 (2020) 153073

Contents lists available at ScienceDirect

Journal of Alloys and Compounds

journal homepage: http://www.elsevier.com/locate/jalcom

Structural and electron transport properties of $CaFe_2O_4$ synthesized in air and in helium atmosphere

Yu.V. Knyazev [a, *], A.S. Tarasov [a, **], M.S. Platunov [a, ***], A.L. Trigub [b], O.A. Bayukov [a], A.I. Boronin [c], L.A. Solovyov [d], E.V. Rabchevskii [d], N.N. Shishkina [d], A.G. Anshits [d]

[a] Kirensky Institute of Physics, Federal Research Center KSC SB RAS, 660036, Krasnoyarsk, Russia
[b] NRC "Kurchatov Institute", 123182, Moscow, Russia
[c] Boreskov Institute of Catalysis, Russian Academy of Sciences, Siberian Branch, 630090, Novosibirsk, Russia
[d] Institute of Chemistry and Chemical Technology, Federal Research Center KSC SB RAS, 660036, Krasnoyarsk, Russia

ARTICLE INFO

Article history:
Received 12 August 2019
Received in revised form
11 November 2019
Accepted 17 November 2019
Available online 18 November 2019

Keywords:
$CaFe_2O_4$
Mössbauer spectroscopy
EXAFS/XANES
XPS
Conductivity measurements
Activation energy

ABSTRACT

The samples with the $CaFe_2O_4$-type crystal structure were obtained by the solid-state reaction method at 1000 °C in the air and the helium atmosphere for the first time. We investigated the modification of the structural and electronic properties of the obtained samples. Mössbauer, *XAFS*-, *XPS*-spectroscopies, and *dc*-, *ac*-conductivity measurements were carried out. Mössbauer and *XAFS*-spectroscopies showed that the local environment of Fe and Ca cations does not change in the case of the inert atmosphere synthesis. Nevertheless, a sharp six-order increase in the electrical resistance observed at room temperature for the sample obtained in the in the helium atmosphere. Moreover, calculated from *dc*-conductivity data activation energy rises from 0.327 for the air-synthesized sample to 0.585 eV for helium-obtained one. This behavior indicates significant modification of in-band-gap energy structure, which correlated with thermally activated charge carriers. Our *ac*-conductivity measurements in the frequency range of 1 kHz −2 MHz for the $CaFe_2O_4$ obtained in the air showed the presence of defect levels in the energy band structure. Oxygen pressure reduction during the synthesis results in levels vanishing. Therefore, we suppose the key role of oxygen atoms in the transport properties of the material, which is indirectly confirmed by *XPS* data. In prospect, $CaFe_2O_4$ can be used in promising gas analyzers.

1. Introduction

Some materials with a spinel-type structure under the high hydrostatic pressure transforms into the orthorhombic $CaFe_2O_4$-type crystal structure [1,2]. Such transition accompanied by abrupt electronic properties change. For example, $LiMn_2O_4$ spinel-to-$CaFe_2O_4$-structure deformation leads to the activation energy reduce from 0.40 to 0.27 eV [1]. It was found that the transition to the orthorhombic $CaFe_2O_4$-type structure increases the hopping mobility of such materials. Therefore, a practical application of spinels could be expanded by the high-pressure technique application. Another way to obtain materials with the $CaFe_2O_4$-type crystal structure is the using of alkaline earth metals with a large ionic radius (>1.0 Å) as substituting cations in ferrites (for example, Ca, Ba, Sr). Due to the huge chemical pressure, spinel unit cell transforms into the crystal structure with the orthorhombic syngony (space group *Pnam*) [3–5]. After this transition, Fe^{3+} occupies only octahedral crystallographic sites, while alkaline cations with 2+ valence state have a dodecahedral environment with an oxygen coordination number of eight. In the latter papers, much attention is paid to the electronic properties of Ca-ferrite [6–8]. It was shown that calcium ferrite is a *p*-type semiconductor, and has a rather large specific resistance (~10^2–10^3 Ω·cm) [7,9,10].

Study of lattice oxygen mobility in $CaFe_2O_4$ was carried out in Refs. [7,8,11]. These results suggest that Ca-ferrite and composites based on it could be promising functional materials. For example, as oxygen carriers for producing syngas, biofuels [12,13], in semiconductor devices [14,15] and as highly sensitive oxygen and ozone gas analyzers due to the high activity of the surface [16]. A *p*–*n* junction can be formed with ZnO and WO_3 oxides that give the

* Corresponding author.
** Corresponding author.
*** Corresponding author.
E-mail addresses: yuk@iph.krasn.ru (Yu.V. Knyazev), taras@iph.krasn.ru (A.S. Tarasov), ms-platunov@yandex.ru (M.S. Platunov).

https://doi.org/10.1016/j.jallcom.2019.153073
0925-8388/

prospect of their application as solar energy conversion devices [14,15]. Recently, the possibility of using semiconductor $CaFe_2O_4$ nanorods as an effective reducing agent for organic pollutants was demonstrated [17]. Biocompatibility of the nanocrystalline $CaFe_2O_4$ makes it possible for biomedical application [18,19]. One of the biomedical engineering achievements was reported in a recent paper [20]. The authors produced a novel electrochemical sensor from sonochemically prepared ferrite clusters of $CaFe_2O_4$ and a modified carbon screen-printing electrode. This sensor showed high sensitivity and selectivity for detecting trace amounts of nitrides in food.

Oxygen nonstoichiometry and ionic conductivity of $CaFe_2O_4$-based membranes depend on surface processes, unlike garnets [21]. One of the advantages of gas sensors based on materials with *p*-type conductivity is low dependence on atmospheric humidity, as well as the ability to absorb higher concentrations of oxygen [22]. Thereby, the problem of the electronic properties investigations of the Ca-ferrite at various oxygen partial pressures becomes an urgent task. To the extent of our knowledge, the transport properties of $CaFe_2O_4$ were studied only in the high-temperature range [7,8]. In these conditions, the Fermi level lies near the middle of the bandgap, so the shallow impurity levels energy could not be estimated. Measurements of the *ac*-conductivity of semiconductors at the low temperatures allow us to determine the impurity levels' energy because the Fermi level becomes near to the impurity level [23].

In this work, solid-phase synthesis was used to obtain $CaFe_2O_4$ samples without any significant impurity of other crystal phases. Samples were annealed in an atmosphere with a wide range of oxygen partial pressure to study the effect of electronic properties changes by using Mössbauer, *XPS*-, *XAFS*-spectroscopies at room temperature, as well as *dc*- and *ac*-conductivity measurements in the 77–300 K temperature range.

2. Samples and experimental methods

We used a high purity Fe_2O_3 (heavy metals (Cu, Co, Sb) impurities $< 5.0\cdot10^{-3}$ wt. %) and purity CaO (heavy metals impurities $< 1.0\cdot10^{-2}$ wt. %) oxides to synthesize $CaFe_2O_4$ samples. The Fe_2O_3 content was thoroughly controlled on 74 wt. % of the total reagents' mass, according to the CaO–Fe_2O_3 phase diagram. Reagents in the mentioned proportions were mixed in a ball mill for an hour. The obtained powder was pressed under a pressure of 346 MPa (with an exposure of 1.5–3 min) into pellets with a diameter of 17 mm and a thickness of 1–2 mm. The obtained pellets were annealed at 1000 °C for 4 h in the air (sample 57), in the helium atmosphere (helium content of 99.995 vol %) with a partial pressure of oxygen of 10^{-5} kPa (sample 57–1) and in the additionally cleaned helium through the system *RMSH*-2 (*Agilent Technologies, USA*) (sample 57–2). Calcination was carried out in the isothermal zone of the tubular muffle furnace. To create a helium atmosphere, the furnace quartz pipe was closed from two sides with the possibility of input and output of gas. A helium flow passed through a pipe during annealing. At the output, the gas was discharged through a pipe 3 mm in diameter, 1.5 m long through a water valve. After annealing, all samples were cooled to room temperature with the furnace turned off regime (~8 °C/min).

The quantitative X-ray phase analysis was performed by *X'Pert Pro MPD* powder X-ray diffractometer (*PANalytical, Netherlands*) with *PIXcel* solid-state detector and a secondary graphite monochromator for CoK_α-radiation. The crystal structure parameters were determined and refined using the full-profile Rietveld approach by the derivative difference minimization (*DDM*) method [24].

The transport properties studies were carried out using the four-contact method on the original installation in the temperature range 77–300 K with alternating current in the frequency range from 20 Hz to 2 MHz using an *E4980A* (*Agilent*) *LCR*-meter and with direct current using *SourceMeter 2634B* (*Keithley*) and *Model 6517B* (*Keithley*) [25,26]. For conductivity measurements, we prepared samples of $4 \times 4 \times 1$ mm^3 in size. Well-conductive contacts were deposited with silver epoxy adhesive H20S (*Epotek*).

Mössbauer spectra of the samples were measured using standard MS1104Em spectrometer in the constant acceleration mode with the 512-channels detector. A mobile source of ^{57}Co(Rh) gamma-ray photons was at room temperature. Experimental samples were fixed in a polymer iron-free holder so that the sample was perpendicular to the propagation direction of gamma rays. Interpretation of the spectra was performed in two stages. At the first stage, we determined the probability distribution of quadrupole splitting P(QS) in the spectrum. Such calculation gives possible nonequivalent iron positions in the samples.

To perform the P(QS) calculation, the experimental spectrum was filled by a number of doublets with Lorentzian line-form and natural line-width (W = 0.24 mm/s for ^{57}Co(Rh) source) and QS with the step Δ = 0.01 mm/s (in our case, from 0.00 mm/s to 1.0 mm/s). Then, the isomer shift and intensity of Mössbauer lines were varied. As a result, we obtained the set of the intensities corresponding to each doublet in our series. These data conform to the probability of each doublet existence in the experimental spectrum.

Then, based on these calculations, we formed a preliminary spectrum. It is contained a set of Mössbauer doublets, corresponding to possible nonequivalent positions and modeling as a group of the analytical functions. This group was fitted to the experimental spectrum by varying the entire set of hyperfine parameters using the least-squares method in the linear approximation (χ^2 criterion). Mössbauer absorption lines were represented by the pseudo-Voight function, following the equation

$$I = I\left(\frac{\mathrm{k}}{(1+x_i)^2} + (1-\mathrm{k})\cdot e^{-\ln 2\cdot x_i^2}\right)$$

Here, $x_i = 2\cdot\left(\frac{IS-i}{W}\right)$, i – is a channel number. *I*, *IS* and *W* are hyperfine parameters (line intensity, Isomer shift and line-width, respectively), k – is the Lorentz-Gauss parameter, which determines the absorption line form. In our case the approximation of the Lorentz form was used, i.e. k = 1.

X-ray absorption fine structure (*XAFS*) spectra in the near (*XANES*) and extended (*EXAFS*) regions at the Fe *K*-edge were recorded in the transmission mode at room temperature at the Structural Materials Science beamline (National Research Center "Kurchatov Institute", Moscow). For the selection of the primary beam photon energy, Si(111) channel-cut monochromator was employed, which provided an energy resolution of $\Delta E/E \sim 2\cdot10^{-4}$. The ΔE scanning step was about 0.4 eV and 0.5 eV in the *XANES*- and *EXAFS*-region, respectively. Scanning in the *EXAFS*-region was carried out at a constant step on the photoelectron wave number scale with $k = 0.05$ Å^{-1}. Signal accumulation time was 4 s per each point. The *EXAFS*-spectra were normalized to an edge jump and the absorption coefficient of the isolated atoms. After subtraction of the smooth atomic background, the conversion from *E* to *k* scale was performed. The k^2-weighted *EXAFS* function was calculated in the intervals $k = 2$–12 Å^{-1} using the Kaiser-Bessel window. The *EXAFS* structural analysis was performed using theoretical phases and amplitudes as calculated by *FEFF*-8 package, and the experimental data fitting was carried out in the *R*-space with the *IFFEFIT* software package [27,28].

X-ray photoelectron spectra (*XPS*-spectra) were obtained using the *ES*-300 photoelectron spectrometer (*KRATOS Analytical*). The anode voltage and emission current of the X-ray tube were 13 kV and 13 μA, respectively. The electrostatic analyzer was operated in the constant pass energy transmission regime. Samples were pre-cleaned by an argon gun for the layer-by-layer analysis of the surface in the preparation chamber. Then the samples were moved into the analyzer chamber using a standard metallic holder. A well-conductive adhesive tape provided the electrical contact of the sample with the metal holder. This method of sample deposition did not create any impurities under the X-ray beam action at room temperature. Spectrometer calibration was performed using bulk gold (Au4$f_{7/2}$) and copper (Cu2$p_{3/2}$) photoelectron lines with the binding energy values of 84.0 and 932.7 eV, respectively. The spectra calibration was made relatively C1*s* peak from carbon admixtures on the oxide surfaces using reference binding energy 285.0 eV.

3. Results and discussion

3.1. X-ray diffraction and Mössbauer spectroscopy

The room temperature X-ray patterns of the samples are shown in Fig. 1. All patterns demonstrate peaks at the same angle θ, corresponding to the $CaFe_2O_4$ crystal structure. According to the X-ray difference spectrum (see curve 3 for sample 57 in Fig. 1), all samples exhibit only one crystallographic phase of $CaFe_2O_4$ with a small admixture of 1% of the hematite. This well agrees with the phase diagram of the $CaO–Fe_2O_3$ system [29]. The $CaFe_2O_4$ crystal structure is orthorhombic with the space group *Pnam*. Unit cell parameters and volume for all samples are shown in Table 1. These values are consistent with the previous data [4,7,8]. It is seen that the unit cell volume is slightly decreasing for samples obtained in the helium atmosphere. The crystal structure of the Ca-ferrite has two nonequivalent crystallographic iron sites with quite a different distortion degree of the oxygen octahedrons around the Fe-atoms (Fe1 and Fe2 inset of Fig. 1) [4,7]. The Fe1 site is substantially more distorted than the Fe2 one [7,8]. The changes of these distortions for samples 57, 57–1 and 57–2 were studied by Mössbauer effect measurements at room temperature in detail.

The Mössbauer spectra of the samples and calculated

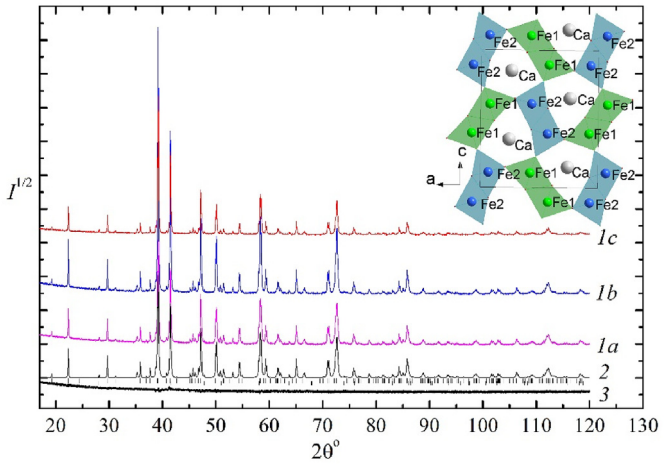

Fig. 1. Room temperature X-ray diffraction pattern of the samples. Experimental patterns for sample 57 (1a), 57–1 (1b) and 57–2 (1c). Calculated (2) pattern and the difference curve (3) are shown for sample 57. The inset shows the crystallographic unit cell of $CaFe_2O_4$.

Table 1
Unit cell parameters of the samples obtained by X-ray diffraction.

Sample	*a*, Å	*b*, Å	*c*, Å	*V*, Å^3
57	9.2257	3.0201	10.6995	298.112
57–1	9.2271	3.0192	10.6999	298.083
57–2	9.2264	3.0192	10.6995	298.049

quadrupole splitting distribution P(QS) are shown in Fig. 2. The probability distribution of quadrupole splitting P(QS) clearly shows two well-separated peaks for all samples, which correspond to the two nonequivalent iron sites (Fe1 and Fe2) in the Ca-ferrite crystal structure mentioned above. The inert atmosphere synthesis does not lead to defective iron sites formation. In other words, $CaFe_2O_4$ demonstrates a stable local atomic structure that is in agreement with the data of [7]. However, we observed a change of the peak's symmetry (mainly for Fe2) which indirectly indicates variations in the iron local atomic structure and crystallographic distortions in the vicinity of iron atoms.

Mössbauer spectra demonstrate a combination of two quadrupole doublets with the parameters collected in Table 2. Isomer shift (IS) values over all samples are almost constant and correspond to octahedrally coordinated Fe^{3+} state in both nonequivalent positions. There is no evidence of other charge states of iron. Because of it and the electroneutrality principle, we can say, that Ca cations must have 2+ valence state. Therefore, synthesis in the helium atmosphere does not affect the electron density and oxygen coordination of the iron. The stability of the iron isomer shift value reveals that the metal-oxygen bond lengths are constant and manifests in the valence stability of the Ca cations. Moreover, it is clear that the lattice oxygen loses are absent in our synthesis conditions.

The distortions of the local atomic structure around the Mössbauer nuclei is the origin of the quadrupole splitting of the Mössbauer doublet. The local distortions arise from the crystalline field asymmetry; the asymmetry degree is determined by the electric field gradient (EFG) value. Such dependence represented by the following equation of the quadrupole splitting (ΔE_Q):

$$\Delta E_Q = \frac{e}{4} Q \cdot V_{zz} \sqrt{1 + \frac{\eta^2}{3}}$$

Here, *Q* is the quadrupole moment of the iron nucleus, V_{zz} is the main component of the electric field gradient tensor, η is the asymmetry parameter of the EFG tensor. Since the *Q* is the constant, the main component of EFG V_{zz} only affects the quadrupole splitting of the Mössbauer doublets. In such an approach, we estimated the relationship between the EFG value in Fe1 and Fe2 positions. EFG value of the Fe1 is about 2.5 times higher than in Fe2 sites.

Despite the above-mentioned lattice oxygen stoichiometry, Mössbauer parameters in Table 2 (see "Area" column) demonstrate a presence of the iron vacancies in all samples with the $CaFe_2O_4$ crystal structure [8,30]. The difference of the doublet area equals 8% for samples obtained both in the air and helium atmosphere. Besides, a slight rise of the line-width (W) for Fe2 sites (Table 2) is observed. Regardless of the synthesis conditions, the number of vacancies has a constant value and evidence of the high stability of Ca-ferrite structure. Taking into account our P(QS) data, we may note a very slight effect of the inert atmosphere conditions on the local symmetry of the iron. Therefore, the local environment of iron atoms depends on the inert atmosphere synthesis only within the Mössbauer line-width limits that could be varies in the range of ~10^{-7} eV.

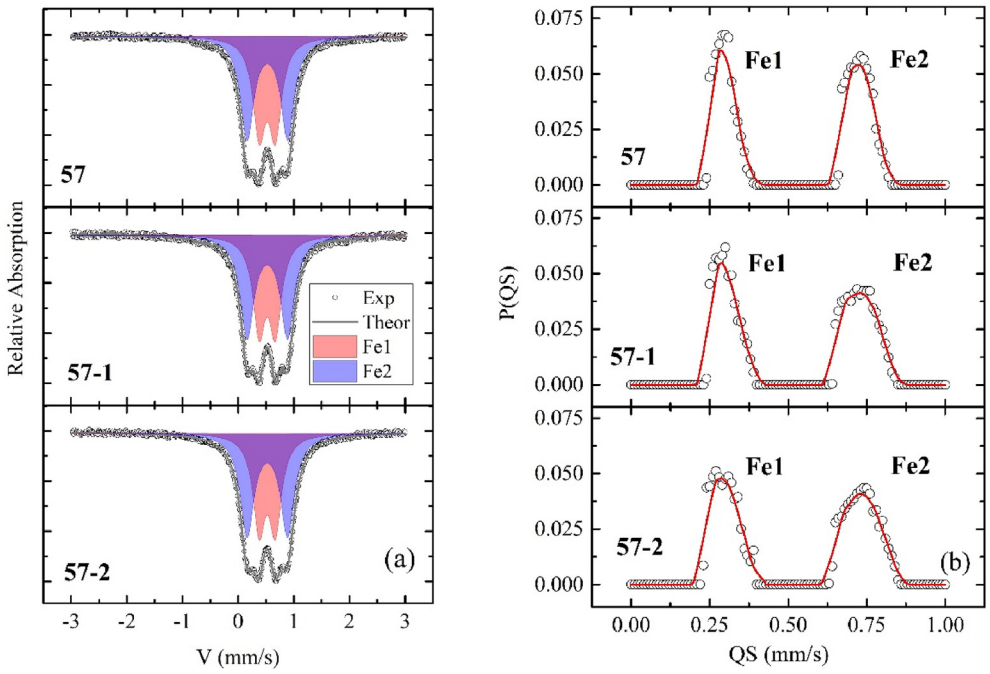

Fig. 2. (a) Mössbauer experimental spectra shown by dots, the fitting indicated by the solid lines. The filled patterns show the doublets of the Fe1 (red) and Fe2 (blue) positions of iron. (b) The distribution of quadrupole splitting P(QS) probabilities shown by the empty circles (with the step of 0.01 mm/s). The solid lines show the approximation of the calculated data. (For interpretation of the references to colour in this figure legend, the reader is referred to the Web version of this article.)

Table 2
Mössbauer parameters of $CaFe_2O_4$. IS is the chemical isomeric shift relative to α-Fe, QS is the quadrupole splitting, W is the width of the Mössbauer line at half-height, Area designates the relative occupancy of the position.

Sample	IS, mm/s ±0.005	QS, mm/s ±0.02	W, mm/s ±0.02	Area, ±0.03	Position
57	0.368	0.73	0.29	0.54	Fe1
	0.367	0.29	0.27	0.46	Fe2
57−1	0.368	0.73	0.29	0.54	Fe1
	0.367	0.29	0.28	0.46	Fe2
57−2	0.367	0.73	0.29	0.54	Fe1
	0.365	0.29	0.31	0.46	Fe2

3.2. XAFS (XANES and EXAFS) spectroscopy

The normalized *XANES*-spectra of the samples measured at room temperature at the Fe *K*-edge is presented in Fig. 3. For all spectra, there are main features: the electronic transition from the iron 1s ground state to subbands constructed from hybridized Fe(3*d*)-O(2*p*)-Fe(4*p*) states (A feature) near the bottom conduction band and to bands with the dominant Fe(4*p*) nature hybridized with the states O(2*p*) (peaks B and C). The pre-edge feature A in the range of 7110−7118 eV corresponds to the $1s \rightarrow 3d$ transition, which is forbidden in the dipole approximation). This transition manifest s itself due to the *d*/*p* orbital mixing. The shape and intensity of the pre-edge feature correlate with the distortion degree of the coordination octahedron and are an indicator of the Fe^{3+} ion in low-symmetric configurations.

The energy of the center of the $1s \rightarrow 3d$ transition (feature A) for all samples is similar and indicates that the iron formal charge state is close to 3+, which is in agreement with our Mössbauer data. The spectral peak C at 7132 eV corresponds to the dipole-resolved main transition $1s \rightarrow 4p$ for Fe^{3+}. In the *XANES* spectra, a shoulder is observed near 7122 eV (feature B). This feature is related to the charge transfer process from the ligand to the Fe-cation. This process is accompanied by a multielectron transition $1s3d^{n+1}4p^1L^1$ with charge transfer from the ligand to the levels of Fe(3*d*). These

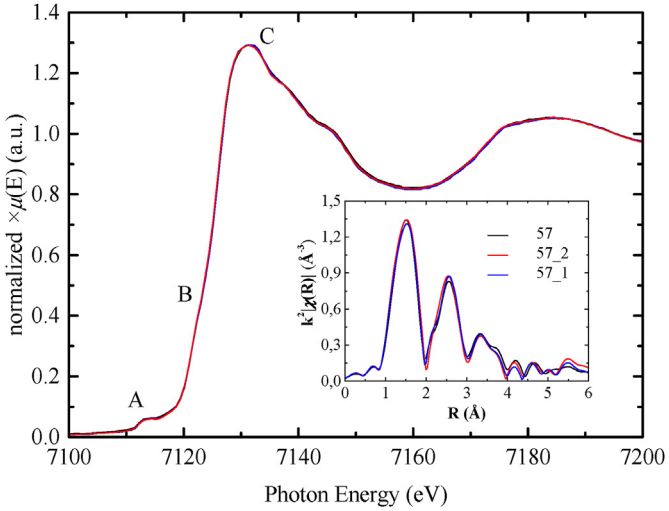

Fig. 3. Normalized *XANES*-spectra of the samples measured at the Fe *K*-edge at room temperature. Inset: Fourier-transforms obtained from the *EXAFS*-spectra.

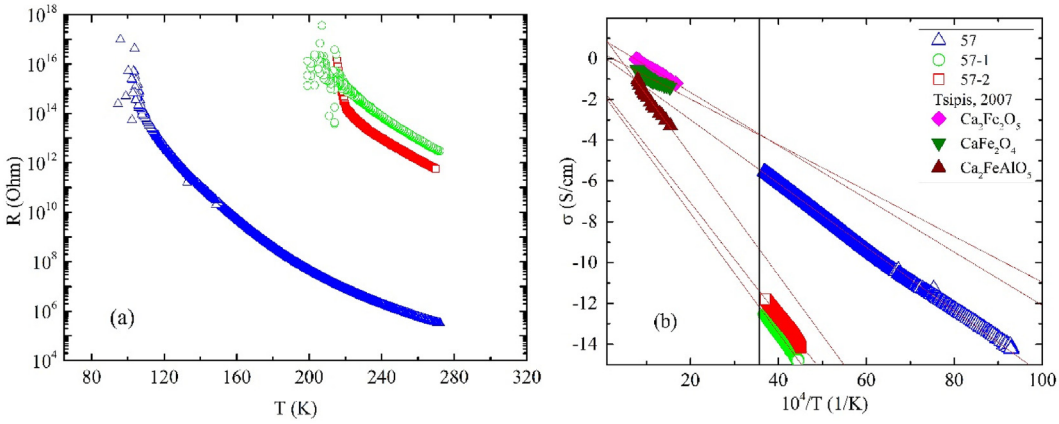

Fig. 4. (a) Measured temperature dependence of the resistance of the $CaFe_2O_4$ samples. (b) The temperature dependences of conductivity in the logarithmic scale and, for comparison, the results of *Tsipis* et al. [7] are shown. The vertical line indicates the room temperature region.

transitions are lower in energy than the main transition, and their intensity depends on the covalence degree of this site. It is important to note that the direct overlap between Fe(3*d*) orbitals is small, and O(2*p*) oxygen orbitals, which directly participate in indirect exchange interaction, can contribute to O(2*p*) → Fe(3*d*) transitions with charge transfer. The *XANES* and *EXAFS* spectra of all samples are similar in shape and practically do not demonstrate differences in the intensity and energy position of the spectral features. Thus, similar coordination of iron ions for all samples is observed, which confirms Mössbauer data.

3.3. Conductivity study and XPS

A general view of the *R*(*T*) dependence of the samples is typical for ferrites [31] and shown in Fig. 4a. The typical temperature behavior for semiconductors is observed. However, the resistance reaches high values already at room temperature (especially for samples 57−1 and 57−2) and rises with temperature decrease. At the same time, sample 57−1 reveals a kink on the *R*(*T*) curve in the vicinity of 230 K. This may indicate an additional transport mechanism below 220 K. Unfortunately, for the 57−1 and 57-2 samples below the temperature of 200 K measurements cannot be performed, due to the extremely high resistance (~10^{16} Ω).

All curves well obey the linear law in the Arrhenius coordinates, which indicates a thermal activation type of conductivity. It is clearly seen from Fig. 4b, that Ca-ferrite *dc*-conductivity becomes six-order smaller in the case of the inert atmosphere synthesis. Decrease of the partial oxygen pressure gives the rise of the activation energy (E_A) value from 0.327 eV for sample 57 (obtained in the air) to 0.525 eV and 0.585 eV for samples 57−1 and 57−2, respectively. Since $CaFe_2O_4$ dielectric gap width is about 1.9 eV [32], E_A values could be interpreted as the energy of defects/impurity levels or subzones, which localized in the forbidden band. At high enough temperature the localized charge carriers from such defects/impurity levels transfers to conduction or valance band (electrons or holes, respectively) and starts to participate in the charge transport process. Generally, the formation of the levels in the forbidden zone associated with oxygen defects in a crystal lattice [7,8].

Our measurements show that the activation energy value of the sample 57 correlates with the data obtained by *V. V. Kharton* [8]. According to this paper, the Ca-ferrite activation energy is 0.24 eV in the temperature range of 650−920 K and 0.35 eV in the range of 920−1170 K. Such values are consistent for other spinels with the alkaline cations, for example, $MgFe_2O_4$ [33]. The E_A values for the samples 57−1 and 57−2 correlate with the high-temperature activation energy (0.52 eV) obtained in the range of 1190−1270 K [8].

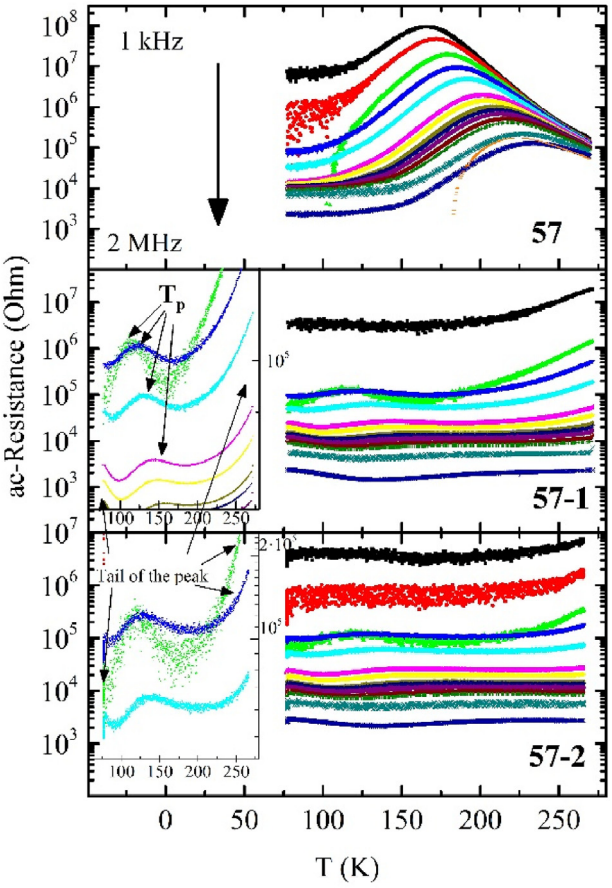

Fig. 5. Temperature dependence of the active resistance at different frequencies of alternating current. The inset shows selected frequencies of *ac*-resistance. Arrows indicate the positions of the peaks and tails.

To refine the transport mechanisms, we measured *ac*-resistance in the temperature range of 77−300 K. Our approach makes it possible to determine the E_A in the high-resistance region, where *dc*-resistance cannot be measured due to instrumental limits. Fig. 5 shows the temperature dependences of the real part of the

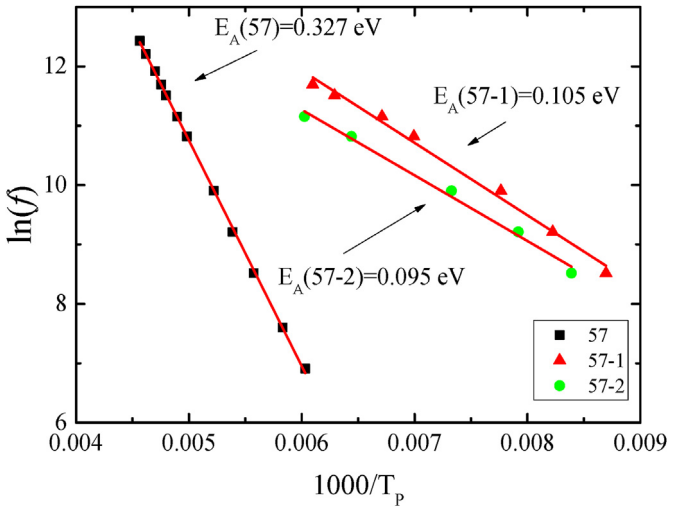

Fig. 6. Temperature dependence of the position of the peak T_P on the frequency *f* for three samples. A solid line shows the linear approximation.

Table 3
Chemical elements content in the samples according to the *XPS* data.

Sample	Concentration, at. %							
	$C_{\sum}$	$C(CO_3)$	$O_{\sum}$	$O(CO_3)$	Fe	$Ca_{\sum}$	$Ca(CO_3)$	Na
57	2.82	0.24	3.79	0.72	1.00	0.46	0.24	0.11
57−1	1.74	0.23	3.19	0.70	1.00	0.39	0.23	0.10

impedance (active resistance) at different frequencies of alternating current (from 1 kHz to 2 MHz) for three samples. For the sample 57, one can see the pronounced peak, which temperature (T_P) depends on the current frequency. We obtained the activation energy [23] from ln(f) of 1000/T_P dependence (Fig. 6), as the slope angle of the straight line. From this view, E_A amounted of 0.327 eV for the 57 sample, which exactly coincides with the value calculated by *dc*-measurements.

Both *ac*-dependencies for samples 57−1 and 57−2 indicate one peak and two "tails of the peak", which could not be distinguished in the available temperature range. The high-temperature "tail" most likely corresponds to E_A = 0.525 eV and E_A = 0.585 eV, obtained from *dc*-data analysis. The calculation for the main peak gives energy about 0.1 eV for both samples (Fig. 6), but the energy of the low-temperature "tail" cannot be estimated. Nevertheless, it can be assumed that at least three types of charge carriers with different activation energies are present in the samples obtained the helium atmosphere. It should be noted that the main contribution to the conductivity comes from charge carriers activated from levels with E_A = 0.525 eV, revealed from the *dc*-resistance. Consequently, in the forbidden band the localized levels with the energy of 0.525 eV have a higher concentration and could define the transport properties of $CaFe_2O_4$.

To clarify the key role of oxygen atoms in the conductivity process, we carried out the measurements of X-ray photoelectron spectra of the samples 57 and 57−1 in the range of 0−1150 eV. Table 3 represents *XPS* data of all observed impurities on the samples' surface. These elements were registered in the regime of the accurate accumulation of the narrow energy regions. In such an analysis, we used areas under the curve that corresponds to observed chemical elements on the surface. Our data show that such concentrations are too small to make an abrupt change of the conduction properties. Moreover, overall impurities are almost equal for both samples. Therefore, observed abrupt conductivity decline and activation energy rise are the phenomena appropriated to the samples itself.

The representative spectra in the range of oxygen binding energy for samples 57 and 57−1 are shown in Fig. 7. We performed the curve-fitting analysis using Lorentz-Gauss approximation to decompose integral of the O1s lines. For quantitative analysis, the areas under the corresponding peaks and atomic sensitivity factors given in the literature [34,35] were used.

The spectra of the O1s lines for both samples demonstrate three oxygen states with the binding energy *E*(O1*s*) ~ 529, 531 and ~532 eV. The state with the *E* ~529 eV refers to the lattice oxygen (OI). Two other states with the binding energy of 531 eV and ~532 eV can be attributed to oxygen states induced by vacancies (OII) and interstitial oxygen (OIII), respectively [36,37]. As it is seen from Fig. 7, inert atmosphere synthesis results in the slight decrease

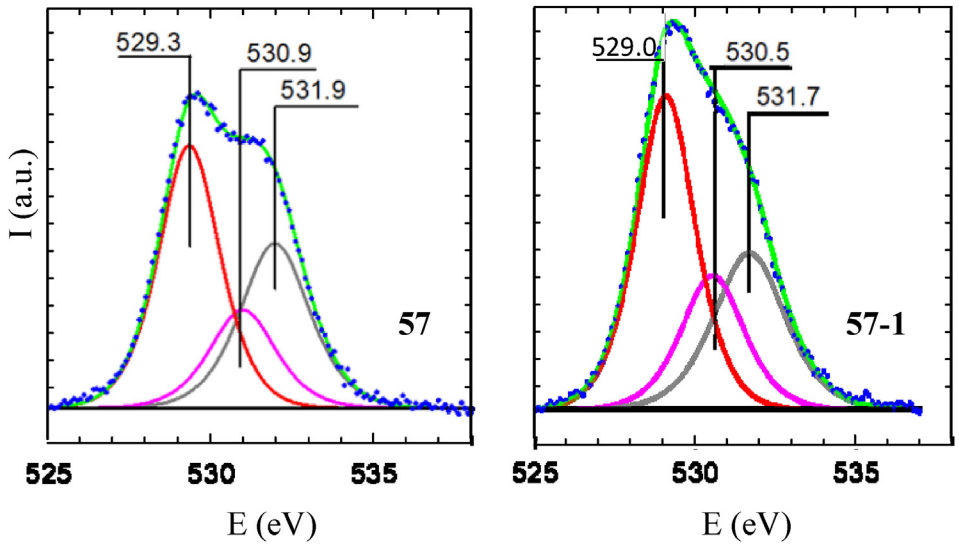

Fig. 7. *XPS*-spectra of the O1*s* line obtained for $CaFe_2O_4$ sample (57) and obtained in the inert atmosphere sample (57−1). Three oxygen states with different binding energies are shown.

Table 4
Relative concentrations of oxygen states (species) of 57 and 57-1 samples.

Sample	Intensity Ratio		
	OII + OIII/OI	OII/OI	OIII/OI
57	1.11	0.40	0.71
57−1	1.07	0.46	0.61

of the binding energy for all oxygen species. Therefore, a helium atmosphere synthesis leads to some ionization of the cation-oxygen bonds. The quantitative analysis shows two noticeable features in comparison to the O1*s* spectra of these samples. First, following data of Table 4, synthesis in an inert ambient decreases the concentration of oxygen species bound to the defects of the lattice (OII and OIII) relatively to OI lattice oxygen. Also, we observe the lattice oxygen (OI) concentration rise compared with other oxygen states. Second, the strong oxygen redistribution between all three forms is observed, with the redistribution between oxygen forms II and III is expressed most strongly. The observed behavior indicates the defect vanishing in the case of inert atmosphere synthesis.

Taking into account our transport measurements, we assumed that sample 57 reveals an oxygen deficiency, and these defects form levels with $E_A = 0.327$ eV. The synthesis in the helium atmosphere leads to oxygen redistribution. As a result, the concentration of defective oxygen states (interstitial and vacant) correlates with electronic transport in $CaFe_2O_4$. Therefore, that, the synthesis in the helium atmosphere leads to the electronic structure change, which we refer to as losses of the oxygen interstitial or vacancy atoms.

4. Conclusion

Our Mössbauer and *XAFS*-spectra indicate that the orthorhombic $CaFe_2O_4$-type crystal structure is stable in low-oxygen pressure synthesis. Transport measurements show a key role of the oxygen atoms in the charge carriers' formation in $CaFe_2O_4$. An inert atmosphere synthesis results in the abrupt increase of the resistance by six orders at room temperature. A lattice oxygen deficiency decreases in the helium atmosphere synthesis. Because of it, $CaFe_2O_4$ reveals the charge localization and the activation energy rise almost twice (from 0.327 eV to 0.585 eV). We associate localized level with $EA = 0.327$ eV ($CaFe_2O_4$ obtained in the air) with the defective (vacancy or interstitial) oxygen. The significant decrease in the concentration of such levels reveals in the helium atmosphere synthesis used. Therefore, oxygen pressure reduction during the synthesis leads to partially removing the defective interstitial oxygen. This does not lead to a change in the charge state of the Ca and Fe cations, but drastically affects the transport properties of the material. Such an effect can be explained by the electron displacement over the chemical bond Me−O and the appearance of temporary electric charges.

Credit author statement

Yu. V. Knyazev: Writing - Original Draft, Methodology, Data Curation, Investigation, Conceptualization, Project administration, Funding acquisition, Visualization, Writing - Review & Editing. A. S. Tarasov: Investigation, Data Curation, Funding acquisition, Visualization, Writing - Original Draft, Software, Writing - Review & Editing. M. S. Platunov: Writing - Original Draft, Software, Funding acquisition, Investigation, Software. A. L. Trigub: Investigation, Software. O. A. Bayukov: Formal analysis, Software, Validation, Writing - Review & Editing. A. I. Boronin: Investigation, Writing - Original Draft, Software. L. A, Solovyov: Investigation, Software. E. V. Rabchevskii: Resources, Investigation. N. N. Shishkina: Resources, Writing - Original Draft. A. G. Anshits: Conceptualization, Validation, Writing - Review & Editing, Supervision.

Declaration of competing interest

The authors declare that they have no known competing financial interests or personal relationships that could have appeared to influence the work reported in this paper.

Acknowledgments

The reported study was partially supported by the Russian Foundation for Basic Research, Government of Krasnoyarsk Territory, Krasnoyarsk Regional Fund of Science (grant #18-42-243011) and the UMNIK Program.

References

[1] K. Yamaura, Q. Huang, L. Zhang, K. Takada, Y. Baba, T. Nagai, E. Takayama-Muromachi, Spinel-to-CaFe2O4-Type structural transformation in LiMn2O4 under high pressure, J. Am. Chem. Soc. 128 (2006) 9448−9456, https://doi.org/10.1021/ja0612302.
[2] Á.M. Arévalo-López, A.J. Dos Santos-García, E. Castillo-Martínez, A. Duran, M.Á. Alario-Franco, Spinel to $CaFe_2O_4$ transformation: mechanism and properties of β-$CdCr_2O_4$, Inorg. Chem. 49 (2010) 2827−2833, https://doi.org/10.1021/ic902228h.
[3] F.P. Glasser, L.D. Glasser, Crystal chemistry of some AB_2O_4 compounds, J. Am. Ceram. Soc. 46 (1963) 377, https://doi.org/10.1111/j.1151-2916.1963.tb11755.x.
[4] B.F. Decker, J.S. Kasper, The structure of calcium ferrite, Acta Crystallogr. 10 (1957) 332, https://doi.org/10.1107/S0365110X5700095X.
[5] C. Do-Dinh, E.F. Bertaut, J. Chappert, Étude par rayons X. Diffraction neutronique et effet Mössbauer du monoferrite de baryum Fe_2O_3-BaO, J. Phys. (Paris) 30 (1969) 566, https://doi.org/10.1051/jphys:01969003007056600.
[6] K. Obata, Y. Obukuro, S. Matsushima, et al., Electronic structure of $CaFe_2O_4$ with antiferromagnetic spin ordering, J. Ceram. Soc. Jpn. 121 (2013) 766, https://doi.org/10.2109/jcersj2.121.766.
[7] E.V. Tsipis, Y.V. Pivak, J.C. Waerenborgh, et al., Oxygen ionic conductivity, Mössbauer spectra and thermal expansion of $CaFe_2O_{4-\delta}$, Solid State Ion. 178 (2007) 1428, https://doi.org/10.1016/j.ssi.2007.09.003.
[8] V.V. Kharton, E.V. Tsipis, V.A. Kolotygin, et al., Mixed conductivity and stability of $CaFe_2O_{4-\delta}$, J. Electrochem. Soc. 155 (2008) P13, https://doi.org/10.1149/1.2823458.
[9] Y. Matsumoto, J. Hombo, F. Nitta, Oxygen sensitivity of a Pt-Pd/p-type $CaFe_2O_4$ diode, J. Appl. Phys. 66 (1989) 5109, https://doi.org/10.1063/1.343743.
[10] Y. Matsumoto, M. Obata, J. Hombo, Photocatalytic reduction of carbon dioxide on p-type $CaFe_2O_4$ powder, J. Phys. Chem. 98 (1994) 2950, https://doi.org/10.1021/j100062a035.
[11] V.V. Yumashev, N.P. Kirik, N.N. Shishkina, Y.V. Knyazev, A.M. Zhizhaev, L.A. Solovyov, Composition, structure and reduction reactivity of composite materials of the α-Fe_2O_3-$CaFe_2O_4$ system by hydrogen, J. Sib. Fed. Univ. Chem. 1 (2019) 54−72, https://doi.org/10.17516/1998-2836-0108.
[12] D. Hirabayashi, T. Yoshikawa, Y. Kawamoto, et al., Characterization and applications of calcium ferrites based materials containing active oxygen species, Adv. Sci. Technol. 45 (2006) 2169. https://doi.org/10.4028/www.scientific.net/AST.45.2169.
[13] Bao-jin Xue, Luo Jia, Fan Zhang, Biodiesel production from soybean and Jatropha oils by magnetic $CaFe_2O_4$−$Ca_2Fe_2O_5$-based catalyst, Energy 68 (2014) 584, https://doi.org/10.1016/j.energy.2014.02.082.
[14] C. Shifu, Z. Wei, L. Wei, et al., Preparation, characterization and activity evaluation of p−n junction photocatalyst p-$CaFe_2O_4$/n-ZnO, Chem. Eng. J. 155 (2009) b466, https://doi.org/10.1016/j.cej.2009.07.009.
[15] R. Wan, C. Jia, W. Zhang, Preparation and photoelectric properties of p-$CaFe_2O_4$/n-WO_3 composites, J. Alloy. Comp. 544 (2012) 1, https://doi.org/10.1016/j.jallcom.2012.07.134.
[16] Y. Matsumoto, F. Nitta, J. Hombo, et al., Oxygen and Ozone Sensitivities of Pt-Pd/p-type $CaFe_2O_4$ and Pt-Pd/n-type TiO_2 Diodes, J. Electrochem. Soc. 138 (1991) 1701, https://doi.org/10.1149/1.2085857.
[17] X. Liu, J. Jiang, Y. Jia, A. Jin, X. Chen, F. Zhang, H. Han, Visible light-responsive carbon-decorated p-type semiconductor $CaFe_2O_4$ nanorod photocatalyst for efficient remediation of organic pollutants, Chin. J. Catal. 38 (10) (2017) 1770, https://doi.org/10.1016/S1872-2067(17)62888-2.
[18] L. Khanna, N.K. Verma, Biocompatibility and superparamagnetism in novel silica/$CaFe_2O_4$ nanocomposite, Mater. Lett. 128 (2014) 376−379, https://doi.org/10.1016/j.jechem.2016.03.019.
[19] L. Khanna, N.K. Verma, Synthesis, characterization and in vitro cytotoxicity study of calcium ferrite nanoparticles, Mater. Sci. Semicond. Process. 16 (2013) 1842−1848, https://doi.org/10.1016/j.mssp.2013.07.016.

[20] P. Balasubramanian, R. Settu, S.M. Chen, T.W. Chen, G. Sharmila, A new electrochemical sensor for highly sensitive and selective detection of nitrite in food samples based on sonochemical synthesized Calcium Ferrite ($CaFe_2O_4$) clusters modified screen printed carbon electrode, J. Colloid Interface Sci. 524 (2018) 417–426, https://doi.org/10.1016/j.jcis.2018.04.036.
[21] V.V. Kharton, A.L. Shaula, E.N. Naumovich, N.P. Vyshatko, I.P. Marozau, A.P. Viskup, F.M.B. Marques, Ionic transport in $Gd_3Fe_5O_{12}$-and $Y_3Fe_5O_{12}$-based garnets, J. Electrochem. Soc. 150 (2003) J33, https://doi.org/10.1149/1.1574810.
[22] S.-W. Choi, A. Katoch, J.-H. Kim, S.S. Kim, Remarkable improvement of gas-sensing abilities in p-type oxide nanowires by local modification of the hole-accumulation layer, ACS Appl. Mater. Interfaces 7 (2015) 647–652, https://doi.org/10.1021/am5068222.
[23] S. Dueñas, I. Izpura, J. Arias, L. Enriquez, J. Barbolla, Characterization of the DX centers in AlGaAs: Si by admittance spectroscopy, J. Appl. Phys. 69 (1991) 4300–4305, https://doi.org/10.1063/1.348403.
[24] L.A. Solovyov, Full-profile refinement by derivative difference minimization, J. Appl. Crystallogr. 37 (2004) 743–749, https://doi.org/10.1107/S0021889804015638.
[25] N.V. Volkov, A.S. Tarasov, D.A. Smolyakov, et al., Extremely high magnetic-field sensitivity of charge transport in the Mn/SiO_2/p-Si hybrid structure, AIP Adv. 7 (2017), https://doi.org/10.1063/1.4974876, 015206.
[26] A.S. Tarasov, M.V. Rautskii, A.V. Lukyanenko, et al., Magnetic, transport, and magnetotransport properties of the textured Fe_3O_4 thin films reactively deposited onto SiO_2/Si, J. Alloy. Comp. 688 (2016) 1095–1100, https://doi.org/10.1016/j.jallcom.2016.07.138.
[27] M. Newville, IFEFFIT: interactive XAFS analysis and FEFF fitting, J. Synchrotron Radiat. 8 (2001) 322, https://doi.org/10.1107/S0909049500016964.
[28] S.I. Zabinski, J.J. Rehr, A. Ankudinov, et al., Multiple-scattering calculations of x-ray-absorption spectra, Phys. Rev. B 52 (1995) 2995, https://doi.org/10.1103/PhysRevB.52.2995.
[29] B. Phillips, A. Muan, Phase equilibria in the system CaO-iron oxide in air and at 1 atm. O_2 pressure, J. Am. Ceram. Soc. 41 (1958) 445, https://doi.org/10.1111/j.1151-2916.1958.tb12893.x.
[30] Y.V. Knyazev, N.N. Shishkina, O. Bayukov, et al., Cation distribution in the composite materials of the $CaFe_2O_4$-α-Fe_2O_3 series, J. Struct. Chem. 60 (5) (2019) 763–771, https://doi.org/10.1134/S0022476619050081.
[31] S. Krupička, Physics of Ferrites, 1976 (Russian translation).
[32] Y. Matsumoto, M. Omae, K. Sugiyama, E. Sato, New photocathode materials for hydrogen evolution: $CaFe_2O_4$ and $Sr_7Fe_{10}O_{22}$, J. Phys. Chem. 91 (1987) 577–581, https://doi.org/10.1021/j100287a018.
[33] J. Smit, H.P.J. Wijn, Ferrites, Philips technical library, Eindhoven, The Netherlands, 1959, p. 278.
[34] J.F. Moulder, W.F. Stickle, P.E. Sobol, et al. (Eds.), Handbook of X-Ray Photoelectron Spectroscopy, Perkin-Elmer Corporation, Physical Electronics Division, Eden Prairie Minnesota, 1992.
[35] C.D. Wagner, W.M. Riggs, L.E. Davis, et al. (Eds.), Handbook of X-Ray Photoelectron Spectroscopy, Perkin-Elmer Corporation, Physical Electronics Division, Eden Prairie Minnesota, 1979.
[36] Anshuman Sahai, Navendu Goswami, Structural and optical investigations of oxygen defects in zinc oxide nanoparticles, Ceram. Int. 40 (2014) 14569–14578, https://doi.org/10.1063/1.4917664.
[37] Sushil Kumar Pandey, Saurabh Kumar Pandey, et al., Effect of growth temperature on structural, electrical and optical properties of dual ion beam sputtered ZnO thin films, J. Mater. Sci. Mater. Electron. 24 (2013) 2541–2547, https://doi.org/10.1007/s10854-013-1130-5.